Enhancing bioelectrocatalytic oxidation of gaseous chlorobenzene by introducing transmembrane Ru^{4+}/Ru^{3+}-mediated reversible intracellular electron transfer

Dongzhi Chen [a,b,c], Haoyang Liu [a,b,c], Jianmeng Chen [a,b,c], Yang Yu [a,c,*]

[a] *Zhejiang Key Laboratory of Petrochemical Environmental Pollution Control, College of Petrochemical Engineering and Environment, Zhejiang Ocean University, Zhoushan 316022, China*
[b] *College of Environment, Zhejiang University of Technology, Hangzhou 310032, China*
[c] *National & Local Joint Engineering Research Center of Harbor Oil & Gas Storage and Transportation Technology, College of Petrochemical Engineering and Environment, Zhejiang Ocean University, Zhoushan 316022, China*

ARTICLE INFO

ABSTRACT

Microbial electrolysis cell (MEC) is a cost-effective process to eliminate chlorinated volatile organic compounds. Poor mass transfer and sluggish intracellular electron transfer remain obstacles. To overcome these, a Ru-mesoporous TiO_2/macroporous carbon (Ru-MeT/MaC) bio-anode was tailored here. The hierarchically meso-macroporous structure separated biofilm formation and chlorobenzene adsorption, improving chlorobenzene mass transfer. Further, modifying Ru created a reversible intracellular electron transfer pathway by introducing transmembrane Ru^{4+}/Ru^{3+} redox couple within bacteria. Such a unique transmembrane introduction induced a compelling bacteria-electricity synergism accompanied by the acclimation of dual-functional genera (degrader & exoelectrogen), promoting the decomposition of aromatic compounds toward organic acids. Those features enabled the resulting MEC to exhibit a super-prominent chlorobenzene elimination capacity (136.7 g m^{-3} h^{-1}) with a short empty bed residence time (60 s), superior to those of state-of-the-art bioelectrocatalytic processes reported. Leveraging the reversible electron transfer, the Ru-MeT/MaC bio-anode was operated in the charging-discharging mode to further enhance chlorobenzene removal.
Synopsis: The concept of introducing bioavailable conductive redox couple into bacteria via reasonably designing the functional structure of the bio-anode is expected to enhance the bioelectrocatalytic oxidation of hydrophobic Cl-VOCs and therefore alleviate air pollution.

1. Introduction

Volatile organic compounds (VOCs), vital precursors causing atmospheric pollution such as photochemical smog and haze, impose a great threat to human health and ecological security [1,2]. As an important type of VOCs, chlorinated VOCs (Cl-VOCs) produce high emissions and high toxicity; therefore, it is crucial to control such gaseous pollutants effectively [3]. Though elegant advances have been achieved for Cl-VOC removal via adsorption, membrane separation, combustion, catalytic oxidation, and biotreatment, these approaches are still formidably challenged by low efficiency, onerous conditions, and high cost, which motivates a continuous search for a more cost-effective process [3–7]. Recently, there has been growing interest in the microbial electrolysis

cell (MEC), a hybrid process coordinating biological and electrochemical advantages, such as electro-assisted biodegradation and bio-alleviated power consumption [8].

The utilization of MEC, however, in eliminating Cl-VOCs is in the inception, and two critical bottlenecks have gradually emerged: (1) Mass transfer of Cl-VOCs is rather poor. Mass transfer is the prerequisite for Cl-VOCs removal. To obtain a satisfactory removal, efficient mass transfer should be guaranteed. Universally, gaseous Cl-VOCs need to first be dissolved in the solution and then diffused toward the biofilm, i. e., a complete mass transfer should sequentially pass through gas-liquid-biofilm phases. But due to the hydrophobicity of most Cl-VOCs, the gas-liquid mass transfer is rather poor. Adsorptive bio-anode is a feasible solution, as hydrophobic Cl-VOCs can be directly captured via adsorption, skipping the problematic gas-liquid mass transfer [9,10]. However,

Nomenclature

MEC	Microbial electrolysis cell.
Ru-MeT/MaC	Ru-mesoporous TiO_2/macroporous carbon bio-anode.
VOCs	Volatile organic compounds.
Cl-VOCs	Chlorinated volatile organic compounds.
MOFs	Metal-organic frameworks.
S_{BET}	Specific surface area.
CB	Chlorobenzene.
DMF	N, N-dimethylformamide.
RF	Resorcinol-formaldehyde.
EBRTs	Empty bed residence times.
IL	Inlet loading.
EC	Elimination capacity.
RE	Removal efficiency.
CE	Current efficiency.
TOF	Turnover frequency.
SEM	Scanning electron microscope.
TEM	Transmission electron microscope.
EDS	Energy dispersive spectrometer.
CLSM	Confocal laser scanning microscope.
XRD	X-ray diffractometer.
XPS	X-ray photoelectron spectroscope.
DPV	Differential pulse voltammetry.
CV	Cyclic voltammetry.
SL	Service life.
GC	Gas chromatographs.
GC-MS	Gas chromatograph-mass spectrometer.
Q_{max}	The maximum adsorption capacity.
ICP-MS	Inductively coupled plasma-mass spectrometer.
IC	Ion chromatograph.
R_{ct}	The bio-anode-solution interface resistance.
$R_{biofilm}$	The biofilm resistance.
C_t	The total electron carrier concentration.
D_{et}	The electron transfer coefficient.
LD_{50}	Median lethal dose.
C_r/C_t	The ratio of reductive electron carrier to total electron carrier.
OCP	Open-circuit potential.
$j_{initial}$	The current peak.
j_{end}	The plateau value.
Q_t	The total discharging charge.
Q_c	Capacitive charge.
Q_{nc}	Non-capacitive charge.
$C \leftrightarrow P$	The polarization modes were switched between constant and pulsation.
$C \rightarrow P$	The constant mode was switched into pulsation mode.
$Q_{pulsation}/Q_{constant}$	The ratio of the total charge between pulsation and constant.
PCA	Principal component analysis.
RDA	Redundancy analysis.
EIS	Electrochemical impedance spectroscopy.

the simultaneous biofilm formation on the bio-anode will compete with Cl-VOCs for adsorption sites, reducing the adsorption efficacy of the bio-anode. Consequently, it is important to separate Cl-VOCs adsorption and biofilm formation sites. (2) Intracellular electron transfer remains sluggish. Biodegradation is the kernel for Cl-VOC removal, where electron transfer within the bio-anode can be regarded as the driving force. The rapider the electron transfer, the stronger the biodegradation capability. Nonetheless, Cl-VOCs possess C-Cl bonds with extreme bio-impedance, which retard electron transfer [11]. Conductive additives, e. g., graphene, carbon nanotube, etc., are fascinating modifications. These modifications can intercalate among anodic bacteria through reasonable design, speeding the extracellular electron transfer [12]. Nevertheless, as they are not bio-available and restricted from access to intracell, the intracellular electron transfer, where the membrane-related cytochrome is dominated, remains sluggish [13]. In other words, the intracellular electron transfer limits the overall electron transfer.

To solve the bottleneck (1), we endeavor to establish a hierarchically meso-macroporous-structured bio-anode, wherein mesopores and macropores function as the Cl-VOC adsorption and biofilm formation sites, respectively. For macroporous materials, porous carbons have gained popularity by virtue of their adjustable porous structure [14]. By using proper templates, macropore size can be well-controlled, which is beneficial for providing abundant proper-sized sites for biofilm formation, alleviating bacteria coverage on adsorption sites. For mesoporous-structured materials, derivatives of metal-organic frameworks (MOFs) stand out since they not only reserve the enormous specific surface area (S_{BET}) of MOFs, providing numerous adsorption sites, but also abandon organic ligands possessing potential bio-toxicity [15]. By combining these two components, a hierarchically meso-macroporous-structured bio-anode can be constructed, beneficial for separating biofilm formation and adsorption, resulting in a more effective mass transfer of Cl-VOCs. On the other hand, the exchangeable characteristic of the internal metal center enables the MOF derivate to be an attractive supporter for further conductive modification. Generally, the Fe^{3+}/Fe^{2+} redox couple functions as the active site in

cytochrome, and an intracellular electron is transferred via successive extraction ($Fe^{3+} + e^- = Fe^{2+}$) and releasing ($Fe^{2+} - e^- = Fe^{3+}$) [16]. Limited by its high standard redox potential (0.77 V), nevertheless, electron extraction is easy but electron releasing is troublesome, i.e., its pseudocapacitive reversibility is rather poor [17]. Inspired by this mechanism, if we modified another similar nature but more reversible redox couple in the MOF derivate, with this redox couple being capable of entering intracell, bottleneck (2) may be addressed. Ru is an ideal candidate, since it is a cognate of Fe (group VIII), and displays analogous properties [18]. Hence, it is postulated that Ru can enter intracell in a way similar to that of Fe. Even better, the Ru^{4+}/Ru^{3+} redox couple features zero-approached standard redox potential (0.10 V), which enables it to possess super pseudocapacitive reversibility [19]. On the basis above, Ru modification is prospective to speed up obstinate intracellular electron transfer.

Summarily, a hierarchically Ru-mesoporous TiO_2 (Ru-MeT)/macroporous carbon (MaC) bio-anode, was proposed herein for use in MEC to remove a typical Cl-VOC, chlorobenzene (CB). The major objectives of this work are to demonstrate the resilient CB removal, to validate hierarchically porous structure-dominated mass transfer, to disclose transmembrane Ru^{4+}/Ru^{3+}-mediated reversible intracellular electron transfer, to unravel the bacteria-electricity synergism, and to further explore the possibility of charging-discharging operation for enhancing the CB removal.

2. Materials and methods

2.1. Chemicals and materials

Chemicals and materials are detailed in Text S1.

2.2. Preparation of the hierarchically Ru-MeT/MaC-structured anode

Fig. S1 schematically outlines the preparation procedure of the Ru-MeT/MaC anode, which is described below.

2.2.1. Preparation of Ru-MeT

Ru-MIL-125(Ti), a classical MOF, was prepared via the hydrothermal-ion exchange two-step method [20]. Firstly, terephthalic acid (1.0 g) and tetrabutyl titanate (0.5 g) were dissolved in a solution containing N, N-dimethylformamide (DMF, 18 mL) and methanol (2 mL). The mixture was stirred for 30 min, poured into a 100 mL Teflon-lined autoclave, maintained at 150 °C for 72 h, and then cooled naturally. The resulting MIL-125(Ti) was separated via centrifugation, washed with DMF and methanol, and dried at 80 °C. Secondly, MIL-125 (Ti) (1.0 g) was immersed in a $RuCl_3$ solution (1.2 g/L, 60 mL) and stirred for 12 h. The resulting Ru-MIL-125(Ti) was separated by filtration, washed with deionized water, and dried at 80 °C.

Ru-MeT was prepared via the pyrolysis method [21]. Briefly, Ru-MIL-125(Ti) was placed in a tube furnace and pyrolyzed at 600 °C for 0.5 h under N_2 protection. The same procedure was applied to prepare MeT but without Ru modification.

2.2.2. Preparation of MaC

MaC was prepared via the soft-template method [22]. Soft-template polystyrene microspheres (3–6 μm, 2.0 g) were dissolved in a solution containing deionized water (9 mL) and ethanol (11 mL), and stirred for 30 min. Subsequently, 1, 6-diaminohexane (0.1 g), resorcinol (3.0 g), and formaldehyde (15 mL) were added to the mixture, stirred for another 30 min, sealed, and heated at 90 °C for 4 h. The resulting polymer, RF resin (resorcinol-formaldehyde), was dried at 90 °C for 48 h, and pyrolyzed at 800 °C for 2 h in a tube furnance under N_2 protection to remove the soft-template.

2.2.3. Preparation of the Ru-MeT/MaC anode

The Ru-MeT/MaC anode was prepared via the spraying method [23]. Ru-MeT and MaC (v/v: 1:1) were homogeneously mixed in a vibrational mill. The mixed powders were suspended in a solution containing Nafion-117 solution (50 μL), isopropanol (2 mL), and deionized water (4 mL). The resulting suspension was spray-coated onto both sides of a graphite (total area 6 cm²) at a loading of 5 mg cm⁻². Finally, the anode was dried at 80 °C to evaporate solvents.

2.3. Operation of MEC

A membrane-separated electrochemical cell consisting of a prepared anode, a platinum cathode, and an Ag/AgCl reference electrode was employed (Fig. S2). The anodic and cathodic chambers were filled with 60 mL of mineral medium with its composition presented in Table S1. The gaseous CB was carried by a portion of air in a stripping jar, homogenized with another portion of air in a mixing jar, and then entered into the anodic chamber. Meanwhile, the electrochemical cell was supplied with electricity using an electrochemical workstation (VSP300, Biologic, France). The anodic chamber was inoculated with the aerobic sludge from a benzene homologs wastewater treatment process (Zhejiang, China), started up by acclimating biofilm, and run at different potentials, empty bed residence times (EBRTs), shock loadings, and starvation times, sequentially (Table S2). Evaluation indicators corresponding to MEC performance, i.e., inlet loading (IL), elimination capacity (EC), removal efficiency (RE), current efficiency (CE), and turnover frequency (TOF), were calculated according to equations in Text S2.

2.4. Abiotic anode and bio-anode characterization

The morphology of the abiotic anode was observed using a scanning electron microscope (SEM, Sigma 300, Zeiss, German) and a transmission electron microscope (TEM, JEM 2100 F, JEOL, Japan), with the elemental distribution and crystalline phase analyzed by an energy dispersive spectrometer (EDS, Xplore 50, Oxford, UK) and an X-ray diffractometer (XRD, Ultima IV, Rigaku, Japan), respectively. The distributions of mesopore and macropore were measured by a static

adsorption instrument (TriStar II Plus, Micromeritics, USA) and a mercury porosimeter (AutoPore IV 9510, Micromeritics, USA), respectively.

The morphology of the bio-anode was observed using a SEM (Nova Nano 450, FEI, USA), a TEM (Tecnai TF30, FEI, USA), and a confocal laser scanning microscope (CLSM, LSM780, Zeiss, German), with the elemental distribution, elemental valence state, and bacterial viability analyzed by an EDS (Super-X, Thermo Scientific, USA), an X-ray photoelectron spectroscope (XPS, AXIS Supra, Kratos, UK), and a live/dead staining assay, respectively. The bacteria number and the dry biomass of the bio-anode were estimated from a hemocytometer counting method and a Bradford method, respectively. The electrochemical behavior of the bio-anode, i.e., electrochemical impedance spectroscopy (EIS), chronocoulometry, cyclic voltammetry (CV), and differential pulse voltammetry (DPV), were analyzed using the electrochemical workstation. The biofilm from the bio-anode was investigated through 16 S rDNA sequencing and metagenomic sequencing, where microbial community structure, genus-environmental variable correlation, genus co-occurrence, and metagenomic functional genes were acquired. The characterization procedures are detailed in Text S3.

2.5. Analysis

CB and CO_2 were quantified using gas chromatographs (GC, 7890B and 8860B, Agilent, USA). Aromatic compounds were identified using a gas chromatograph-mass spectrometer (GC-MS, 7890B-5977B, Agilent, USA). Organic acids and Cl^- were quantified using an ion chromatograph (IC, Aquion RFIC, Dionex, USA). The toxicity of CB and intermediates was evaluated using a toxicity estimation software tool. The Ru element in the bio-anode was quantified using an inductively coupled plasma-mass spectrometer (ICP-MS, NexION 300X, PerkinElmer, USA). The analysis procedures are detailed in Text S4.

3. Results and discussion

3.1. Bio-anode-driven resilient CB removal

Physicochemical properties of the abiotic anode were characterized first. The prepared Ru-MeT well-preserved the typical octahedral-shaped crystal of MIL-125(Ti) [24], along with the successful exchange of the Ru species with the original metal center Ti (corresponding increase/decrease in Ru/Ti content), albeit transforming the original crystalline phase toward corresponding metal oxides, i.e., anatase and ruthenium oxide, as organic ligands were decomposed during pyrolysis (Figs. S3-S4). After milling, Ru-MeT was successfully anchored into MaC, and another set of diffraction peaks corresponding to graphitic carbon was also detected [25], validating that Ru-MeT and MaC were well incorporated with each other (Figs. S4-S5).

It is common knowledge that the anodic potential is vital to MEC, thus CB removal was examined at various potentials. A prominent RE promotion was observed as the potential increased initially to 0.6 V, beyond which only a marginal extra promotion was observed (Fig. 1A). As such, 0.6 V was selected as the optimum potential. Similarly, 1 min was chosen as the optimum EBRT. Despite this delightful electrical stimulation phenomenon, we are still wondering if the bio-anode design is valid. For this reason, two extreme IL step-change scenarios, i.e., shock loading and starvation, were adopted herein. Shock loading can be created by increasing the CB concentration stepwise. It appears that only the Ru-MeT/MaC bio-anode exhibited continuously elevated EC, whereas others were plagued with severe EC recessions under high CB concentrations (Fig. 1B). This indicated that the Ru-MeT/MaC bio-anode was highly resistant to shock loading. Generally, gaseous pollutant removal involves two steps, i.e., mass transfer and biodegradation, and the slower one is deemed as the rate-determining step, which could be ascertained by fitting the EC-IL curve. As shown in Fig. 1C, two major regions separated by a critical IL appeared. The former region, whose ILs were below the critical value, displayed a linearity, insinuating that CB
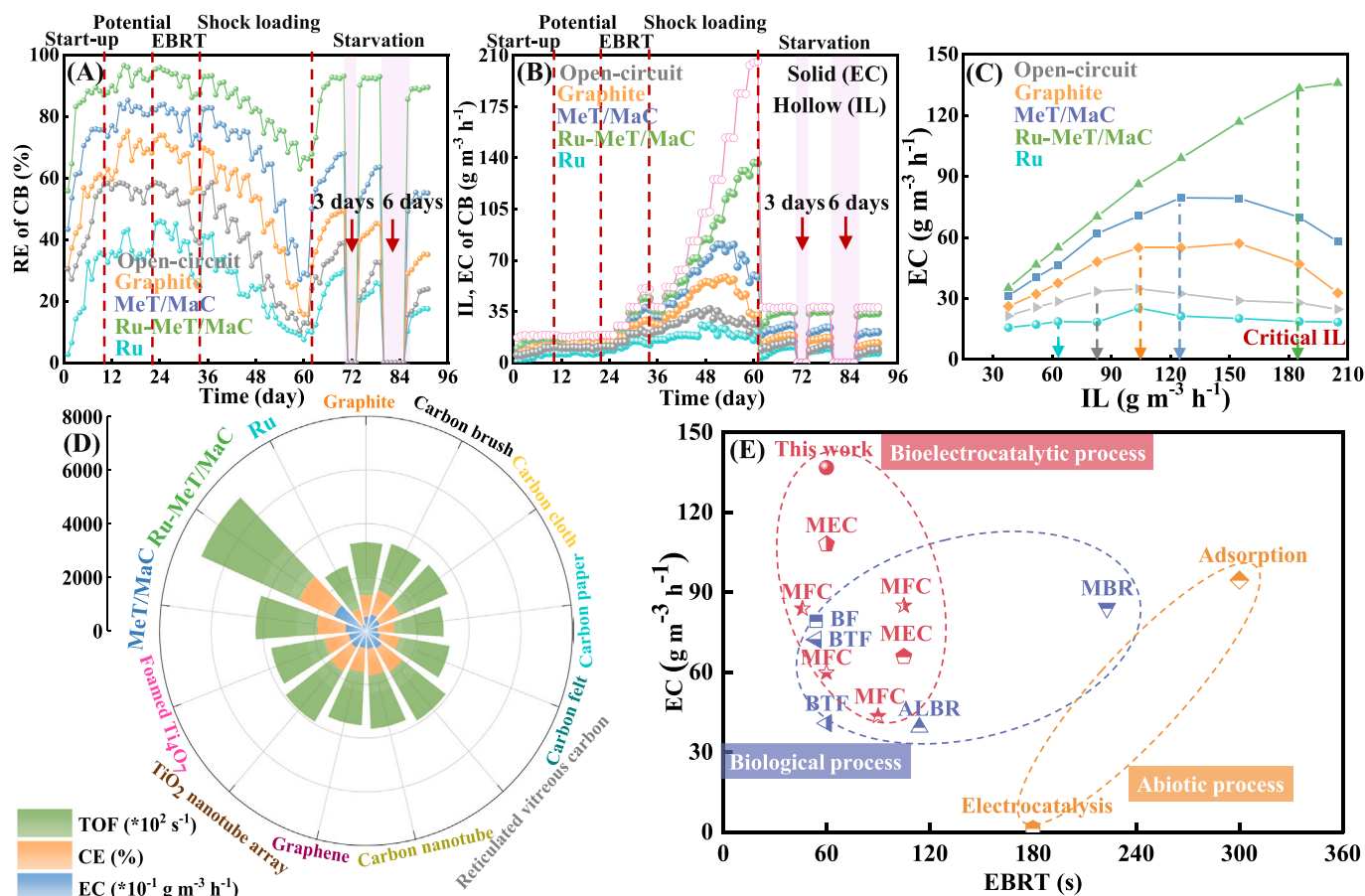
Fig. 1. Time courses regarding (A) RE, (B) IL and EC, and (C) EC-IL curves of CB obtained in MECs using different bio-anodes at potential variation, EBRT variation, shock loading, and starvation stages, with detailed operational conditions presented in Table S2. (D) Nightingale diagram of performance comparison between the Ru-MeT/MaC bio-anode and other laboratory-made bio-anodes used in MEC for CB degradation. Operational conditions: potential = 0.6 V, CB concentration = 0.6 g m^{-3}, and EBRT = 1 min (E) Gaseous pollutant removal performance comparison between this work and other bioelectrochemical, biological, and abiotic processes reported in the literature.

removal was mass transfer controlled; while the latter region, whose ILs were beyond the critical value, came to a standstill or even fell back, insinuating that the biodegradation limitation occurred gradually. Notably, the Ru-MeT/MaC bio-anode presented delayed critical IL along with much higher EC than others, robustly evidencing its strengthened biodegradation. Fig. 1A-1B also show the bio-anode performance under the starvation scenario, which was triggered by periodically cutting down the CB supply. In sharp contrast with others, which displayed deteriorated RE and EC confronting the gradually prolonged starvation, the Ru-MeT/MaC bio-anode exhibited resilient CB removal, accompanied by recoverable CO_2 and Cl^- production (Fig. S6). Taken together, the Ru-MeT/MaC bio-anode was capable of functioning as the electron sink/source to resiliently survive shock loading/starvation, whose mechanism was uncovered in Section 3.3.

In an attempt to further demonstrate the superiority of our bio-anode design, three normalized indicators, EC, CE, and TOF, were calculated and compared among different types of laboratory-made bio-anodes, including conventional carbon-based bio-anodes (graphite, carbon brush, carbon cloth, carbon paper, and carbon felt), emerging carbon-based bio-anodes (carbon nanotube, graphene, and reticulated vitreous carbon), porous titanium dioxide bio-anodes (foamed Ti_4O_7 and TiO_2 nanotube array), and the Ru-MeT/MaC bio-anode prepared herein (Fig. 1D). Thereinto, the Ru-MeT/MaC bio-anode achieved prominent EC, CE, and TOF of 136.7 g m^{-3} h^{-1}, 1478.0%, and 412,844.0 s^{-1}, respectively, considerably higher than those obtained in conventional carbon-based ones (46.3–65.6 g m^{-3} h^{-1}, 660.5%–928.7%, and

181,866.3–202127.5 s^{-1}), emerging carbon-based ones (63.9–76.6 g m^{-3} h^{-1}, 912.7%–1012.8%, and 196,504.8–210050.7 s^{-1}), and porous titanium dioxide ones (68.9–73.3 g m^{-3} h^{-1}, 956.7%–1024.8%, and 209,134.7–217167.1 s^{-1}). What needs to be emphasized here is that a CE greater than 100% is generalized in MEC because a bacteria-electricity synergistic effect was induced (Table S3) [26–32]. With the aid of the Ru-MeT/MaC bio-anode, our MEC, surprisingly, possessed the highest CE among all MECs reported to date. Fig. 1E compares the gaseous pollutant removal performance of this study with bio-electrocatalytic, biological, and abiotic processes reported in the literature, with detailed information presented in Table S3 [33–45]. Evidently, bioelectrocatalytic process was more technically favorable for gaseous pollutant removal than biological and abiotic processes since it possessed higher EC and shortened EBRT. Impressively, Our MEC considerably surpassed reported state-of-the-art bioelectrocatalytic systems using other bio-anodes, which substantially illustrated the technological superiority of the Ru-MeT/MaC bio-anode.

An excellent bio-anode should not only be effective, but also be durable. Hence, the service life (SL) of the bio-anode, which is defined as the operation time at which the Ru content is less than 1%, was investigated (Text S5). After 91-day continuous operation, only 2.1% of the total Ru was lost. Assuming that Ru loss was stable during the subsequent operation, SL of the Ru-MeT/MaC bio-anode was predicted to be 8.8 years. In fact, due to the stable nature of Ru species, SLs of conventional Ru-modified anodes ranged from 4 to 6 years [46,47]. The comparable SL achieved in our study implied that the Ru-MeT/MaC

bio-anode possessed enough durability for long-term use. Additionally, as estimated in Table S4, the unit price of the Ru-MeT/MaC bio-anode was only 881.43 $ m^{-2}, which was cheaper than conventional noble metal oxide-modified anodes (1900–4620 $ m^{-2}) [48,49]. This was ascribed to the porous nature of MeT/MaC, which could provide interlaced Ru anchoring sites and eliminate its agglomeration, accordingly, making the modified Ru to be highly dispersive and saving its dosage. Further, the economic applicability of MEC system was evaluated by cost estimation, as detailed in Text S6. The total cost of MEC was estimated to be 0.021 $ g^{-1} CB, comprising the capital cost (0.0065 $ g^{-1} CB) and operational cost (0.015 and 1.8×10^{-5} $ g^{-1} CB derived from the pumping and DC power energy consumption, respectively). This meant that the pumping energy consumption accounted for most of the total cost, and the addition of the bio-anode and electricity supply only brought about a limited extra cost compared with the conventional biological process, proving the cost-effectiveness of our system.

3.2. Hierarchically porous structure-dominated mass transfer

Mass transfer is the prerequisite for the removal of gaseous pollutant, but due to the hydrophobicity of CB, mass transfer from the bulk gas to biofilm is rather poor. MeT was chosen to pre-capture CB owing to its abundant mesopores and corresponding large S$_{BET}$ for adsorption (Fig. S8 and Table S5). An electricity-free adsorption test was then undertaken, and it appears that the CB adsorption well-followed the Langmuir isotherm pattern (Text S7 and Fig. S9). Clearly, the maximum adsorption capacity (Q$_{max}$) of abiotic MeT reached 19.6 mg g^{-1}, 35 folds that of abiotic graphite (Fig. 2A). We further assessed the CB adsorption of the bio-sample, where covered bacteria were inactivated beforehand

to exclude the simultaneous biodegradation effect. Unfortunately, when MeT was covered with bacteria, Q$_{max}$ suffered a severe reduction (5.4 mg g^{-1}), along with a corresponding decrease in the mesopore volume and S$_{BET}$ (Table S6). Since the size of MeT (0.5–1 μm) was smaller than those of bacteria (1–3 μm) (Fig. 2B and S5), direct coverage of bacteria on MeT would block its mesopores, weakening the subsequent CB adsorption. By contrast, though there was only a minor Q$_{max}$ (6.5–6.8 mg g^{-1}) obtained in MaC, the coverage of bacteria seemed to barely affect the CB adsorption. Different from the mesoporous MeT, since we controlled the size of the soft-template (3–6 μm) similar to or slightly larger than bacteria size during MaC preparation, abundantly ordered macropores (2–8 μm) could be created in MaC (Fig. S8 and Table S5). This not only advantageously provided abundant proper-sized sites for biofilm formation, alleviating the biofilm coverage on mesopores and liberating more mesopores for CB adsorption, but also beneficially formed a thick porous-like biofilm rather than a thin mud-like biofilm of blocked MeT (Figs. S10-S11). Given this, we attempted to incorporate MaC with MeT, and the resulting MeT/MaC featured a hierarchically meso-macroporous structure (Table S5). This allowed biofilm formation and CB adsorption to be confined within macropores and mesopores, respectively. Consequently, a prominent Q$_{max}$ (15.3 mg g^{-1}) was observed even when MeT/MaC was covered by bacteria, with the corresponding exposure of MeT crystals and well-retained mesopores (Fig. 2A-2B and Table S6). Meanwhile, high biomass could still be maintained on the MeT/MaC bio-anode (Fig. 2C). Though the further modification of Ru wouldn not affect either CB adsorption or biomass, the potential antibacterial effect remained suspicious, as reported previously [50]. From Fig. 2D and S12, due to the low content of Ru (2.7%), high bacterial viability could be maintained in
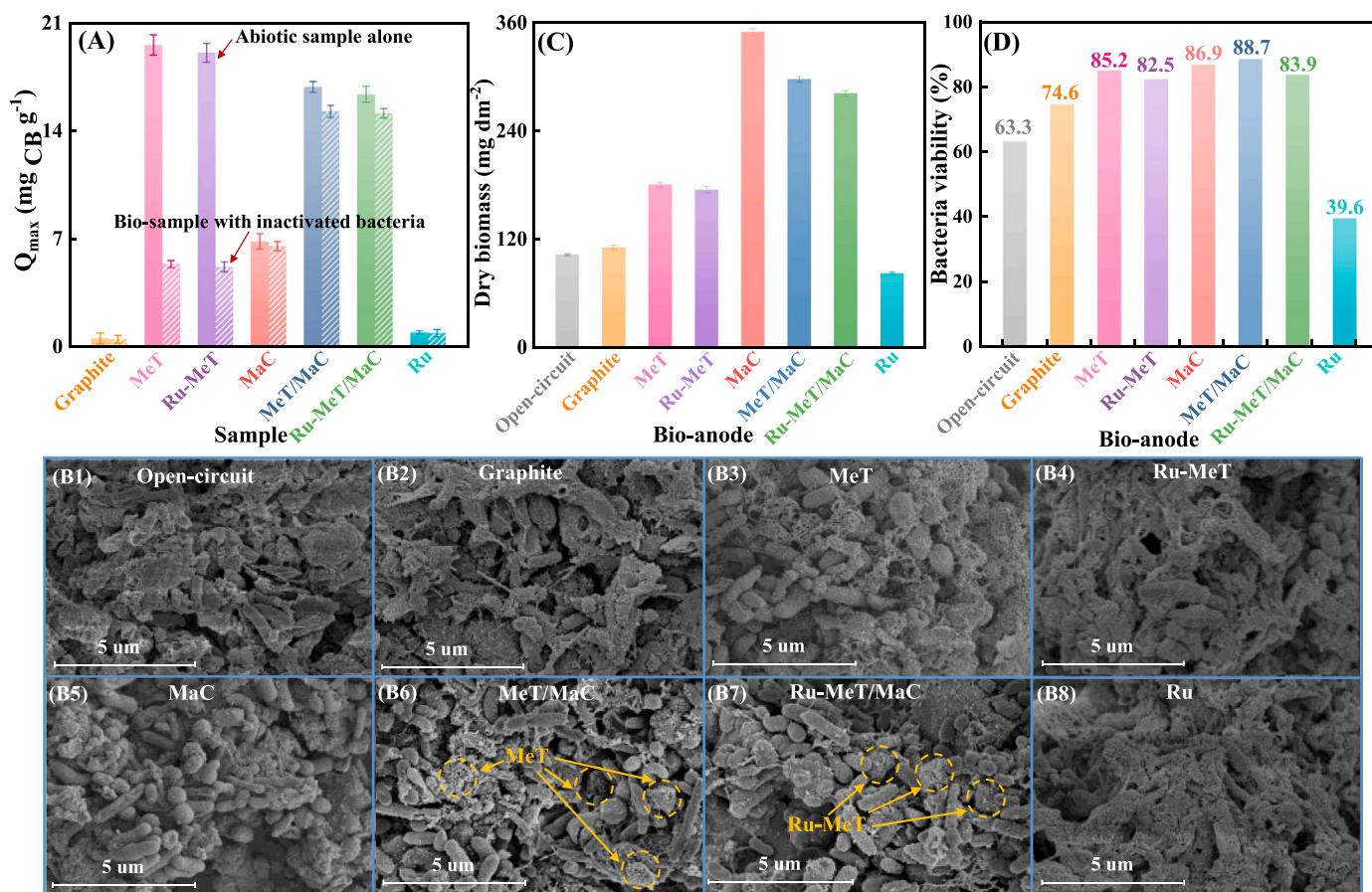

Fig. 2. (A) The maximum adsorption capacity (Q$_{max}$) fitted by Langmuir model of different abiotic samples and bio-samples covered by inactivated bacteria in electricity-free condition. Operational conditions: potential = 0 V, initial CB concentration = 13.2–165 mg L^{-1}, sample dosage = 0.1 g, and adsorption time = 2 h. (B) SEM images, (C) dry biomass, and (D) bacteria viability of different bio-anodes.

the Ru-MeT/MaC bio-anode (83.9%). A significant antibacterial effect (39.6%) occurred only in the pure Ru bio-anode. Overall, the hierarchically porous structure in MeT/MaC was beneficial to separate biofilm formation (macropores) and chlorobenzene adsorption (mesopores), making CB mass transfer more efficacious.

3.3. Transmembrane Ru^{4+}/Ru^{3+}-mediated reversible intracellular electron transfer

Upon recognizing the role of the hierarchically meso-macroporous structure in mass transfer, we further investigated electron transfer in the Ru-MeT/MaC bio-anode. From EIS plots, two semicircles, which represented the bio-anode-solution interface resistance (R_{ct}) and the biofilm resistance ($R_{biofilm}$), respectively, emerged (Fig. 3A). By fitting experimental EIS results with the equivalent circuit model, it was found that $R_{biofilm}$ almost determined the total resistance, as it showed the largest value compared to other resistances (Table S7). Compared with the graphite bio-anode, $R_{biofilm}$ was halved in the MeT/MaC bio-anode, and it could be further reduced after modifying Ru. However, increasing anodic biomass would lead to a deceptive apparent resistance decrease. Thus, summarizing bioconductive as facilitated is still uncertain. To exclude the above interference, the total electron carrier concentration (C_t), which indicated the conductivity per unit biofilm, was then estimated according to the chronocoulometry described in Text S8, and the results are shown in Fig. 3B. Apparently, C_t almost maintained a similar level in both graphite and MeT/MaC bio-anodes, corroborating the false positive conductivity improvement caused by the biomass accumulation in the MeT/MaC bio-anode. In sharp contrast, the Ru-MeT/MaC bio-anode uplifted C_t by 4.7 times, indicating that modifying Ru could improve conductivity unequivocally. Furthermore, CV was performed to probe the electron behavior between the anode and bacteria, and it turned out that a pair of weak redox peaks (0.10/0.16 V vs. Ag/AgCl) assigned to the bacteria redox reaction emerged only when the anode

was covered with the biofilm. Otherwise, only a single intensive hydrogen evolution peak was observed in the abiotic anode (Fig. S13). CB addition intensified the redox peak, especially the oxidation peak, implying a strong electron transfer from CB to the bio-anode (Fig. 3C). Similar results were obtained in DPV curves with the bio-anode under the turnover conditions (with bacteria and CB) showing an intensive oxidation peak (insert of Fig. 3C). It should be noted that the Ru-MeT/MaC bio-anode possessed the negatively shifted and strongest oxidation peak, substantiating its superior electron extraction capability. The electron transfer coefficient (D_{et}) was obtained by fitting the CV oxidation peak current-scan rate relationship (Text S8 and Fig. S14). Compared with the graphite bio-anode, the Ru-MeT/MaC bio-anode enlarged D_{et} by 11.3 times, which authenticated the pivotal role of modified Ru in accelerating electron transfer. To investigate the reversibility of the electron transfer between the anode and biofilm, the charging-discharging experiment was carried out. Charging-discharging could be fulfilled by either manipulating the potential or CB supply, and the former was conducted first. After fully charging at 0 V, the bio-anode was instantly supplied with a positive potential (0.6 V). A responsive RE increase could be observed, accompanied by a sharp discharging current peak (Fig. 3E-3 F). Once the discharging was stabilized, the bio-anode was charged again using a negative potential (−0.6 V). It was found that RE immediately decreased while switching the potential, and finally retraced back to the value similar to that obtained when 0 V was applied. Meanwhile, a corresponding opposite directional charging current peak was clearly visible. This elucidated that the electron transfer within the bio-anode was reversible. Similar to the potential manipulation, CB was continuously supplied until the bio-anode was fully charged, and then this supply was cut down to discharge the bio-anode. All bio-anodes showed a consistent responsive current decrease, but the lag times differed (Fig. 3H). The lag time reflected the duration of the discharging, in other words, the electron storage capacity during prior charging. Obviously, the Ru-MeT/MaC bio-anode
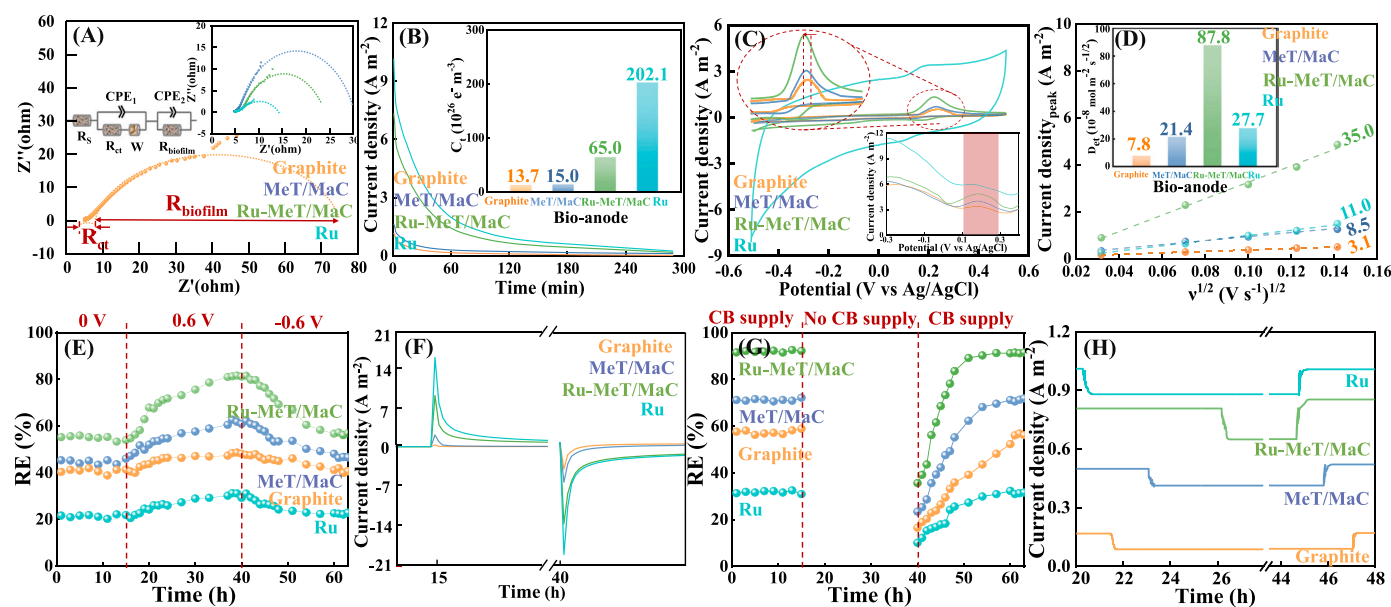

Fig. 3. (A) EIS plots and (B) chronocoulometry experiment (insert is the calculated C_t value) of different bio-anodes under non-turnover conditions (with bacteria and without CB). Operational conditions: applied bias = 0.5 V, sinus amplitude = 10 mV, and frequency range = 10^5-2 Hz for EIS measurement; pre-charging potential = −0.6 V, pre-charging time = 300 s, and discharging external resistor = 1 kΩ for chronocoulometry experiment. (C) CVs (insert is the DPVs) and (D) linear relationship between CV oxidation peak current and the square root of the scan rate as described by Randles−Sevcik equation (insert is the calculated D_{et} value) of different bio-anodes under turnover conditions (with bacteria and CB). Operational conditions: scan window = −0.5 to 0.5 V, scan rate = 1 mV s^{-1}, CB concentration = 0.6 g m^{-3}, and EBRT = 1 min for CV analysis; scan window = −0.3 to 0.4 V, pulse height = 2.5 mV, pulse width = 100 ms, step height = 30 mV, step time = 500 ms, CB concentration = 0.6 g m^{-3}, and EBRT = 1 min for DPV analysis. (E) RE of CB and (F) current density during potential-manipulated charging-discharging. Operational conditions: potential = 0 V (0–15 h), 0.6 V (15–40 h), and − 0.6 V (40–63 h), CB concentration = 0.6 g m^{-3}, and EBRT = 1 min (G) RE of CB and (H) current density during CB supply-manipulated charging-discharging. Operational conditions: potential = 0.6 V, CB concentration = 0.6 g m^{-3} (0–15 h), 0 g m^{-3} (15–40 h), and 0.6 g m^{-3} (40–63 h), and EBRT = 1 min.

possessed the longest lag time, revealing the extensive electron storage capacity in its biofilm. When the current stabilized, the CB supply was restored to recharge the bio-anode, and the Ru-MeT/MaC bio-anode displayed the most sensitive RE recovery (Fig. 3G). Overall, the electron transfer within the Ru-MeT/MaC bio-anode was highly efficient and reversible.

Though highly reversible electron transfer behavior was obtained in the Ru-MeT/MaC bio-anode, the underlying reason behind this phenomenon remained indeterminate. To this end, microbial community structures of bio-anodes were analyzed, and the results at the genus level are shown in Fig. 4A and S15. After long-term electricity-free acclimation, *Enterobacter* became more abundant and finally overwhelmingly dominated the bacterial community in the open-circuit condition (52.9%). When electricity was supplied, however, entirely different taxonomic distribution was observed. Obviously, *Enterobacter* diminished (0.1%), whereas *Pandoraea* became predominant (31.8%). Given this, we evaluated the genus-electricity correlation. An expected negative correlation was witnessed between *Enterobacter* and electricity, whereas a positive correlation was found between *Pandoraea* and electricity (Fig. 4B). Though MeT/MaC literally promoted biofilm formation, it did not significantly affect the microbial community as a similar *Pandoraea* abundance was obtained with that of the graphite bio-anode. With further modification of Ru in MeT/MaC, inerestingly, another genus, *Rhodanobacter* was remarkably enriched (8.5–26.5%), whereas *Pandoraea* still remained in high abundance (40.7%). Again, the correlation heatmap showed a strong positive correlation between *Rhodanobacter* and Ru. Functional genes mediating intracellular electron transfer were analyzed to gain more insights into the role of the foregoing representative genera. As presented in Table S8, three classifications, i.e., cytochrome c oxidase gene, cytochrome cbb3 oxidase gene, and cytochrome bd complex gene, were identified. This was in agreement with the generalized mechanism that the membrane-related cytochrome served as the major intracellular electron transfer mediator within bacteria [9]. These cytochrome-associated genes, conferred with electricity-dependent nature, mainly existed in four genera: *Pandoraea*, *Rhodanobacter*, *Achromobacter*, and *Microbacterium* (Fig. 4C). Besides aforementioned *Pandoraea* and *Rhodanobacter*, *Achromobacter* and *Microbacterium* also showed positive correlations with Ru, albeit with their slightly lower abundances (Fig. 4B). The gene abundance, nonetheless, depended strongly on the bio-anode. Specifically, the Ru-MeT/MaC bio-anode outperformed the graphite bio-anode in upregulating cytochrome-associated genes, particularly the cytochrome c oxidase gene. These jointly elaborated that the Ru modification directionally enriched specific exoelectrogens in conjunction with the simultaneous upregulation of intracellular electron transfer genes.

Is there any driving force, if exists, upregulating intracellular electron transfer genes within the Ru-MeT/MaC bio-anode? To understand this, the ultrathin section of the biofilm from the Ru-MeT/MaC bio-anode was prepared and analyzed via TEM. We found that Ru-MeT/MaC crystals were homogeneously dispersed around isolated bacteria (Fig. 4D). More noteworthy, some Ru species existed inside an individual bacterium, with most of them intriguingly traversing the entire periplasmic space between inner and outer membranes (Fig. 4E and S16). Different from the original metal center of MeT, Ti, which existed solely as Ti^{4+} (Fig. S17), modified Ru species existed as the Ru^{4+}/Ru^{3+} redox couple, which was in agreement with the typical peak locations of
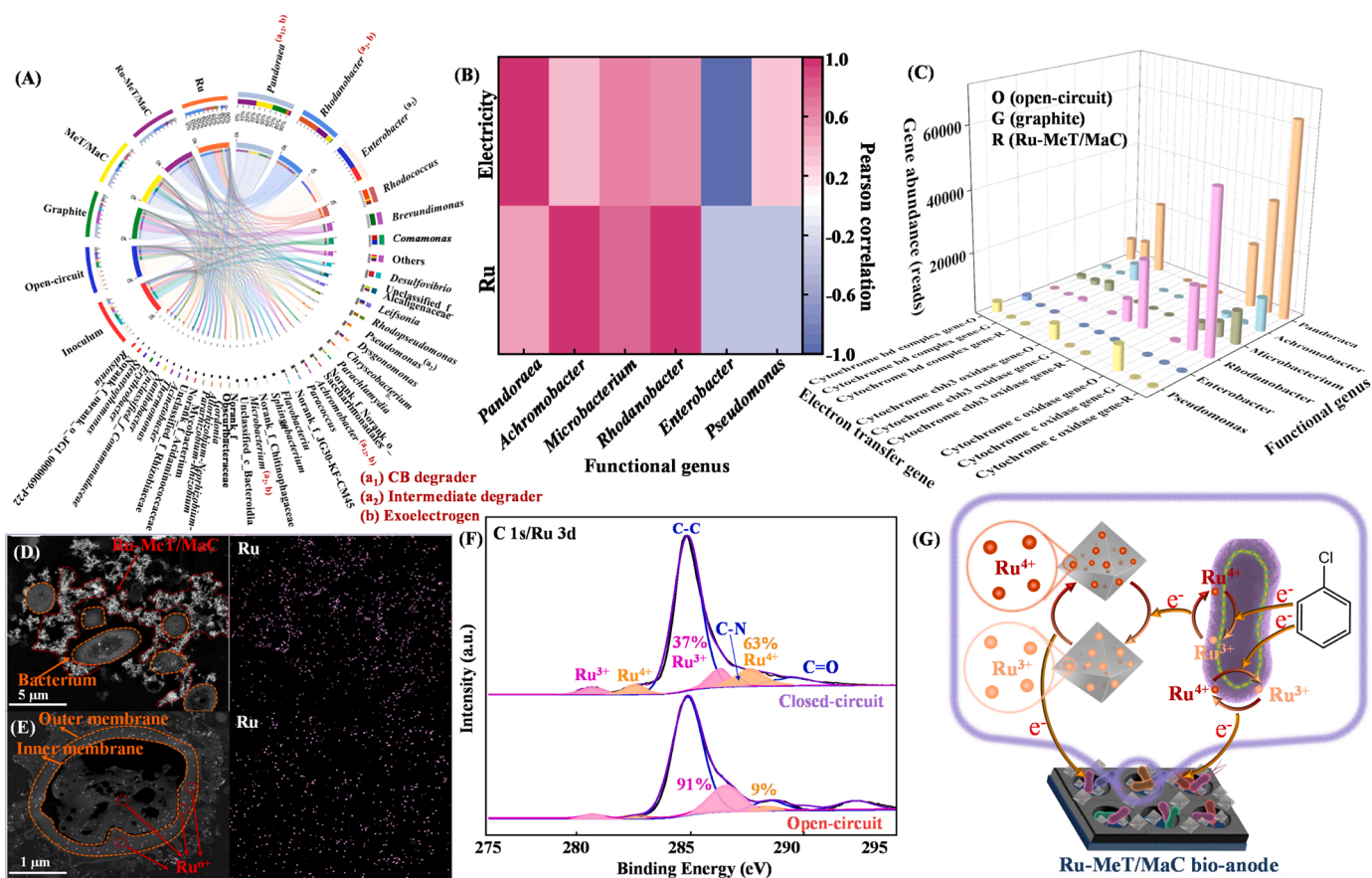

Fig. 4. (A) Microbial community structures of different bio-anodes at the genus level, (B) heatmap correlating functional genus to environmental variables, and (C) taxonomic origins of functional genes associating the cytochrome-mediated intracellular electron transfer. TEM images and corresponding Ru elemental mapping on the ultrathin sections of the (D) bacteria and (E) individual bacterium on the Ru-MeT/MaC bio-anode. (F) Ru 3d XPS spectra of the Ru-MeT/MaC bio-anode in the open-circuit and closed-circuit. (G) Reversible Ru^{4+}/Ru^{3+}-mediated extracellular and intracellular electron transfer in the Ru-MeT/MaC bio-anode.

Ru^{3+} (280.5 and 286.2 eV) and Ru^{4+} (282.5 and 287.7 eV) (Fig. 4F) [51]. Such a redox couple was capable of rapidly extracting electrons from the bacterium in the open-circuit condition with the corresponding $Ru^{4+} + e^{-} = Ru^{3+}$ conversion (Ru^{4+}/Ru^{n+} ratio of 9%), while releasing stored electrons to the external circuit in the closed-circuit condition with the reversal $Ru^{3+} - e^{-} = Ru^{4+}$ conversion (Ru^{4+}/Ru^{n+} ratio elevated to 63%), as evidenced in Fig. 4F. In other words, this Ru^{4+}/Ru^{3+} redox couple was endowed with the reversible pseudocapacitive nature, which enabled it to be a super-efficient electron mediator. Taken together, Ru-MeT/MaC not only produced electronic bridges among bacteria, but more importantly, its modified Ru species could be slowly digested by bacteria to form the unique transmembrane Ru^{4+}/Ru^{3+}, which functioned as the efficacious metallic shortcut to boost the sluggish cytochrome-mediated electron transfer, making the bio-anode to be more conductive, as depicted in Fig. 4G and S18. This, in turn, explained why the Ru-MeT/MaC bio-anode was capable of resiliently surviving shock loading/starvation in Section 3.1, since either the extracellular or intracellular Ru^{4+}/Ru^{3+} were highly reversible in extracting/releasing electrons to offset the external electron donor redundancy/deficiency (Text S9).

3.4. Bacteria-electricity synergism

Leveraging the efficient mass transfer and electron transfer in the Ru-MeT/MaC bio-anode, an impressive synergistic effect between bacteria and electricity might be created. A comparative experiment was, therefore, undertaken to verify the potential synergism. Single biotreatment and abiotic electrocatalysis could be realized by cutting off electricity and inactivating bacteria in MEC, respectively (Fig. 5A). Almost no CB removal was observed by concurrently cutting off electricity and inactivating bacteria in MEC, indicating that the CB adsorption was saturated during continuous operation (data not shown). Clearly, an excellent synergism could be created because a prominent RE of 91.9% was obtained in MEC using the Ru-MeT/MaC bio-anode, much

higher than those of single biotreatment (48.6%) and abiotic electrocatalysis (6.2%). Such a synergism may lead to alternating the CB biodegradation pathway, and consequently, the possible intermediates were monitored in batch mode. As shown in Figs. S19-S20, with the gradual biodegradation of CB, aromatic compounds (2-chlorophenol, 2-chlorohydroquinone, and 1,2,4-benzenetriol) and organic acids (maleic acid, fumaric acid, lactic acid, oxalic acid, and formic acid) sequentially emerged. Through further calculating the stoichiometric carbon/chlorine balance, undefined substances were visualized. From Fig. 5B, the undefined chlorine substance assigned to the transient acyl chloride always maintained a trace level. While the undefined carbon substance displayed a gradually enlarged trend (Fig. 5C). This was attributed to the bacteria anabolism, converting the abiotic carbon toward biocarbon and gradually decreasing the defined carbon. It should be pointed out that the CB removal of the single biotreatment (open-circuit) seemed to stay in the inception phase, with gradually accumulated aromatic compounds. Generally, the efficacy of conventional biotreatment was associated with pollutant bioavailability. For this reason, bioavailability was evaluated by treating intermediates using the unacclimated inoculum, and evidently, aromatic compounds displayed poorer bioavailability than organic acids concerning lower RE and slower biomass growth (Fig. S21A). To make matter worse, these bio-refractory aromatic compounds negatively affected CB removal, with this detrimental effect exacerbated in their higher concentration (Fig. S21B). It was comprehensible because those aromatic compounds were considered to be highly toxic, as they possessed low oral rat LD_{50} and high bio-concentration factor, hampering their further ring cleavage (Figs. S21C-S21D). In the MEC case, nevertheless, those bio-refractory aromatic compounds tended to be further decomposed to biodegradable organic acids, advantageously alleviating the microbial toxicity caused by aromatic compounds (Fig. 5B-5 C). Particularly, there were only trace accumulations of 2-chlorohydroquinone and 1,2,4-benzenetriol, which were proven to be more toxic than the parent CB, when using the Ru-MeT/MaC bio-anode. Further, redundancy analysis (RDA) was
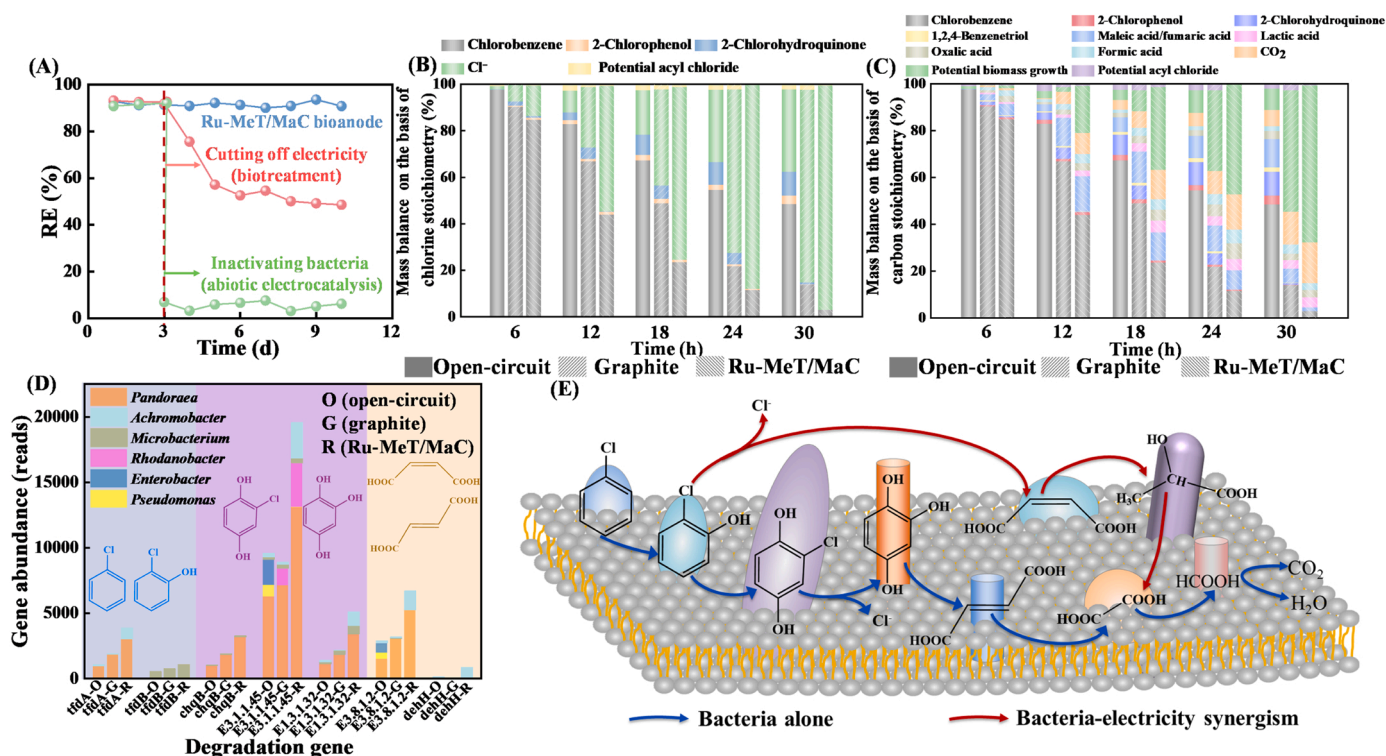

Fig. 5. (A) Synergistic effect between bacteria and electricity. Operational conditions: potential = 0.6 V, CB concentration = 0.6 g m^{-3}, and EBRT = 1 min. Mass balance on the basis of (B) chlorine and (C) carbon stoichiometry. Operational conditions: batch mode, initial CB concentration = 270.8 mg L^{-1}, and potential = 0.6 V. (D) Taxonomic origins of functional genes mediating the targeted pollutant degradation. (E) Ru-MeT/MaC bio-anode enhanced CB degradation pathway.

performed to unravel the degradation selectivity. The intermediate-environmental variable correlation was obtained based on the angle between two vectors, with acute, right, and obtuse angles corresponding to positive, no, and negative correlations, respectively (Fig. S22). There was an appreciable positive correlation between organic acids and Ru, which indicated that the Ru-MeT/MaC bio-anode was conducive to promoting the ring cleavage of aromatic compounds, essentially enhancing the CB removal, as shown in Fig. 5E.

Based on this finding, degradation genes within bacteria were analyzed. Table S9 summarizes the identified degradation genes and their targeted pollutants, with detailed degradation reactions shown in Text S10. It was found that the Ru-MeT/MaC bio-anode significantly upregulated degradation genes, especially for E3.1.1.45 and E1.3.1.32, targeting the degradation of 2-chlorohydroquinone and 1,2,4-benzenetriol, respectively. This explained why almost no accumulation of 2-chlorohydroquinone and 1,2,4-benzenetriol was observed in the presence of the Ru-MeT/MaC bio-anode, since the upregulation of corresponding degradation genes could rapidly convert these bio-refractory aromatic compounds to biodegradable organic acids. More specifically, for single biotreatment, degradation genes primarily originated from three genera, i.e., *Pandoraea*, *Pseudomonas*, and *Enterobacter*, whereinto the latter was substantiated to be abundant in the open-circuit sample (Figs. 4A and 5D). As *Enterobacter* and *Pseudomonas* became less abundant when the Ru-MeT/MaC bio-anode was used, degradation genes originating from these two genera almost faded away, but instead, these

originating from aforementioned exoelectrogens, i.e., *Pandoraea*, *Rhodanobacter*, *Achromobacter*, and *Microbacterium*, could be significantly activated, accompanied by the synchronized activation of ATP hydrolysis genes, uncovering that these exoelectrogens were also dual-functional to serve as CB/intermediate degrader (Fig. 5D and S23). This finding provides new insights into the bioelectrocatalytic process, as exoelectrogen and degrader are generally affiliated with different genera and compete mutually for the ecological niche, which unavoidably lowers the treatment efficacy [52]. Herein, however, the evolution of the special dual-functional genus accidentally mitigated the potential competition between different functional genera, substantially enhancing bacteria-electricity synergism for CB removal.

3.5. Charging-discharging-enhanced CB removal

The reversible electron transfer nature motivates us to speculate if the Ru-MeT/MaC bio-anode can be operated in a potential pulsation mode, in which open-circuit and closed-circuit are used to alternately charge and discharge the bio-anode to further enhance the CB removal. For proof-of-concept, three pulsation times, 2, 5, and 10 min, were adopted. After around 10-day operation, the Ru-MeT/MaC bio-anode in the pulsation mode gradually performed better than that in the constant mode, with higher RE, EC, and CO_2/Cl^- production (Fig. 6A and S24). Particularly, pulsation periods of 5 and 10 min were found to have the best stimulation effect. The anodic potential/current versus time was
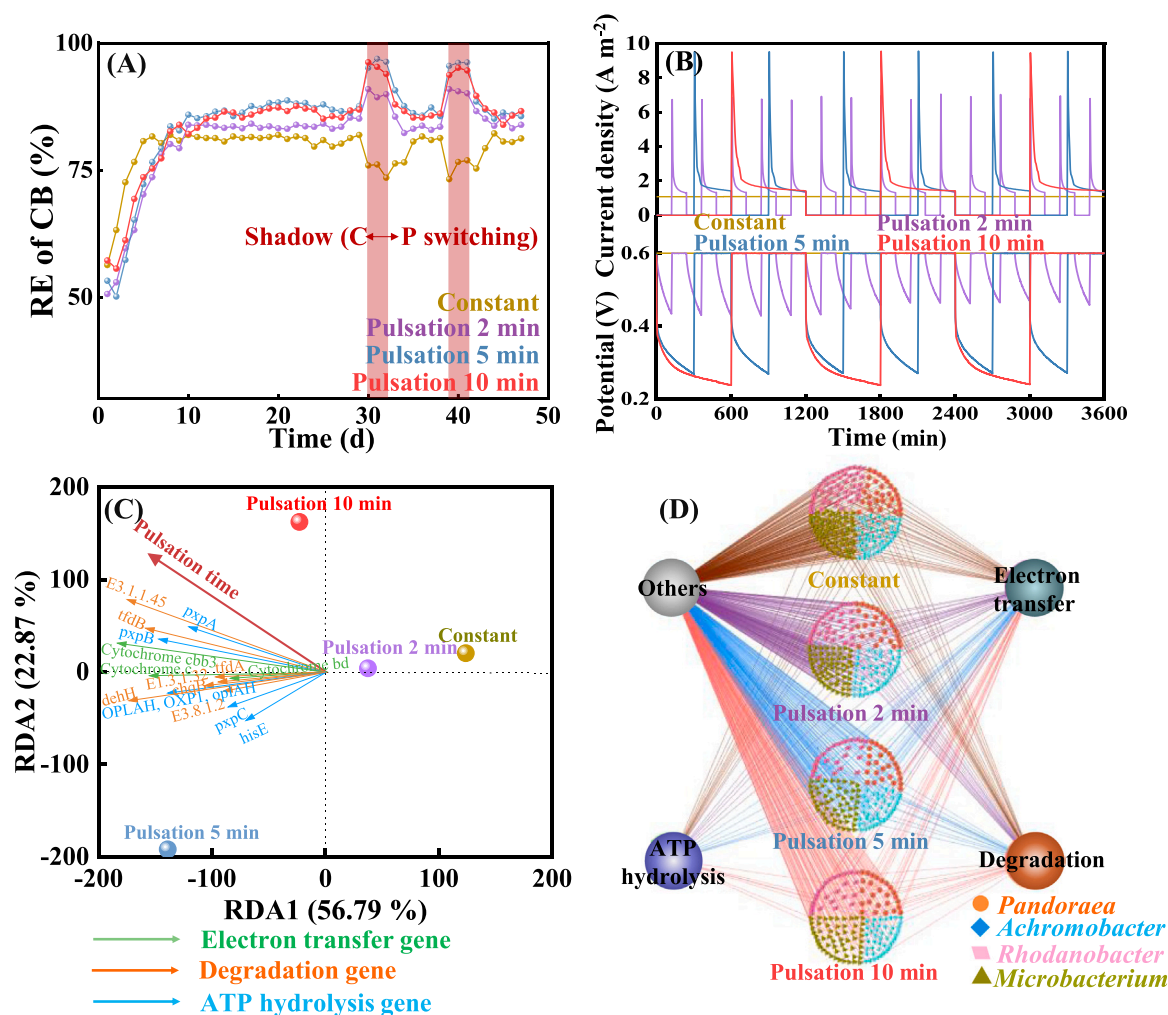

Fig. 6. (A) RE of CB and (B) current density and potential in constant and pulsation modes. Operational conditions: potential = 0.6 V, CB concentration = 0.6 g m^{-3}, and EBRT = 1 min (C) RDA correlating functional genes to pulsation times. (D) Co-occurrence network of dual-functional genus at bio-anodes operated in constant and pulsation modes. Each node represents one independent species OUT affiliated with a certain genus.

then recorded, and different variation patterns were observed between constant and pulsation modes. In comparison with the constant potential/current in the constant mode, a typical charging-discharging behavior was observed in the pulsation mode. During the open-circuit, the current was zero, while the potential decreased gradually (Fig. 6B). This potential decrease was typical to the charging behavior, i. e., electrons were extracted from CB and then stored within the bio-anode, accompanied by its internal redox electron carrier (Ru^{4+}/Ru^{3+}) transforming from the oxidative form (Ru^{4+}) to the reductive form (Ru^{3+}). To quantitatively assess the charging degree, the ratio of the reductive electron carrier to the total electron carrier (C_r/C_t) was calculated based on the open-circuit potential (OCP) variation (Text S11). As displayed in Fig. S25A, as the pulsation period prolonged from 2 to 10 min, OCP decreased initially and subsequently reached a standstill. Correspondingly, C_r/C_t increased initially and then approached a plateau. Obviously, a high charging degree (>92%) was obtained when the pulsation period exceeded 5 min. Right after closing the circuit, a sharp current peak appeared instantaneously. Thereafter, the transient current dropped continuously, finally hitting a plateau (Fig. 6B). This cliff-shaped current curve coincided with the typical discharging behavior, i.e., stored electrons within the bio-anode were released to the external circuit, accompanied by the internal redox electron carrier (Ru^{4+}/Ru^{3+}) transforming back from the reductive form (Ru^{3+}) to the oxidative form (Ru^{4+}). The prolonged pulsation time increased the height of the current peak ($j_{initial}$); however, the plateau value (j_{end}) remained unchanged (Fig. S25B). This indicated that the bio-anode could be discharged entirely, regardless of the charging degree. As such, the total discharging charge (Q_t) could be divided into two parts: capacitive (Q_c) and non-capacitive charge (Q_{nc}) (Text S11 and Fig. S25C). Consistent with the charging results, pulsation periods of 5 and 10 min displayed the highest Q_c and Q_c/Q_t (Fig. S25D).

To explore the possible bacterial acclimation effect caused by pulsation, the polarization modes were switched between constant and pulsation (C↔P) in all MECs for 3 days and then swapped back, as shown in the shadow of Fig. 6A. Although a similar charging-discharging behavior was observed after temporary C→P switching, the detailed performance differed from that obtained through long-term pulsation (Fig. S26). For the sake of accuracy, the MEC performance at the same polarization mode was compared (Table S10). For instance, in the identical constant mode, RE of MEC acclimated in long-term constant was only 81.9%, with a low ratio of the total charge between pulsation and constant ($Q_{pulsation}/Q_{constant}$) of 0.55. In contrast, REs of MECs acclimated in long-term pulsation were 90.9–95.1%, with high $Q_{pulsation}/Q_{constant}$ values of 0.57–0.71. Additionally, more intensive current responses were found in long-term pulsation-acclimated bio-anodes, as shown in CV and DPV curves (Fig. S27). This insinuated there literally existed a bacterial acclimation effect under the pulsation mode. To disclose the microbial community change, principal component analysis (PCA) was performed at the genus level. Although an increasing genus difference was observed between the inoculum and bio-anode over time, a high similarity was always maintained between constant-acclimated and pulsation-acclimated bio-anodes (Fig. S28). Despite the genus similarity, the abundance of functional genes may differ. Indeed, all functional genes, including degradation, intracellular electron transfer, and ATP hydrolysis genes, could be somewhat upregulated through pulsation, especially those originating from *Pandoraea* and *Rhodanobacter* (Fig. S29). As testified in RDA, there was a strong positive correlation between pulsation time and functional genes, and 10 min period posed the most significant impact on gene activation, as its projection point laid the furthest in the pulsation time arrow (Fig. 6C). More importantly, as shown in the co-occurrence network, the occurrence frequency of dual-functional genera, which reflected the diversity of the affiliated species, decreased with the pulsation time (Fig. 6D). This elucidated that although the pulsation only exerted marginal difference at the genus level, it still could specifically screen affiliated species abundant with functional genes.

4. Conclusions

In summary, we established a cost-effective Ru-MeT/MaC bio-anode for CB removal in MEC. MEC using the Ru-MeT/MaC bio-anode exhibited a significant EC of 136.7 g m^{-3} h^{-1} with an EBRT lowered to 60 s, exceeding the values obtained by other bioelectrocatalytic processes reported to date. Further investigation revealed that the hierarchically meso-macroporous structure encouraged the separation of biofilm formation and CB adsorption, promoting CB mass transfer. Additionally, modified Ru was beneficial for creating a highly reversible intracellular electron transfer route by mildly introducing transmembrane Ru^{4+}/Ru^{3+} redox couple within bacteria. This favorably induced a prominent bacteria-electricity synergism along with the directional acclimation of dual-functional genera (degrader & exoelectrogen), e.g., *Pandoraea* and *Rhodanobacter*, thereby leading to the alternation of the CB degradation pathway with bio-refractory aromatic compounds converting to biodegradable organic acids. Furthermore, the reversible electron transfer nature allowed the Ru-MeT/MaC bio-anode to be operated in a charging-discharging mode to further enhance CB removal, with sufficient durability and a low unit price of 8.8 years and 881.43 \$ m^{-2}, respectively. This study highlights the importance of introducing bioavailable conductive redox couple into bacteria by reasonably designing the functional structure of the bio-anode as a means of enhancing bioelectrocatalytic oxidation of Cl-VOCs.

CRediT authorship contribution statement

Dongzhi Chen: Conceptualization, Investigation, Funding acquisition, Writing – original draft. **Haoyang Liu**: Methodology, Investigation, Data duration, Resources. **Jianmeng Chen**: Investigation. **Yang Yu**: Writing – review & editing, Supervision.

Declaration of Competing Interest

The authors declare that they have no known competing financial interests or personal relationships that could have appeared to influence the work reported in this paper.

Data Availability

Data will be made available on request. The data that support the findings of this study are available from the corresponding author upon reasonable request.

Acknowledgment

Appendix A. Supporting information

References

[1] B.C. McDonald, J.A. de Gouw, J.B. Gilman, S.H. Jathar, A. Akherati, C.D. Cappa, J. L. Jimenez, J. Lee-Taylor, P.L. Hayes, S.A. McKeen, Y.Y. Cui, S. Kim, D.R. Gentner, G. Isaacman-VanWertz, A.H. Goldstein, R.A. Harley, G.J. Frost, J.M. Roberts, T. B. Ryerson, M. Trainer, Volatile chemical products emerging as largest petrochemical source of urban organic emissions, Science 359 (2018) 760–764.

[2] W.M. Liu, J.X. Tao, Y.H. Zhao, L. Ren, C. Li, X.F. Wang, J. Chen, J.Q. Lu, D.S. Wu, H.G. Peng, Boosting the deep oxidation of propane over zeolite encapsulated Rh-Mn bimetallic nanoclusters: elucidating the role of confinement and synergy effects, J. Catal. 413 (2022) 201–213.

[3] F.W. Lin, Z. Wang, Z.M. Zhang, L. Xiang, D.K. Yuan, B.B. Yan, Z.H. Wang, G. Y. Chen, Comparative investigation on chlorobenzene oxidation by oxygen and ozone over a MnO_x/Al_2O_3 catalyst in the presence of SO_2, Environ. Sci. Technol. 55 (2021) 3341.

[4] H.Y. Liu, Y. Yu, N.N. Yu, Y.F. Ding, J.M. Chen, D.Z. Chen, Airlift two-phase partitioning bioreactor for dichloromethane removal: Silicone rubber stimulated biodegradation and its auto-circulation, J. Environ. Manag. 319 (2022), 115610.

[5] Y.J. Zeng, X.X. Yang, H. Yu, Birnessite MnO_2 supported on CNTs in-situ for low-temperature oxidation of ethyl acetate, Carbon Res. 1 (2022) 25.

[6] W.M. Liu, S.Y. Yang, Q.L. Zhang, T.Y. He, Y.W. Luo, J.X. Tao, D.S. Wu, H.G. Peng, Insights into flower-like Al_2O_3 spheres with rich unsaturated pentacoordinate Al^{3+} sites stabilizing $Ru-CeO_x$ for propane total oxidation, Appl. Catal. B: Environ. 292 (2021) 120171.

[7] H.G. Peng, T. Dong, S.Y. Yang, H. Chen, Z.Z. Yang, W.M. Liu, C. He, P. Wu, J. S. Tian, T. Peng, X.F. Chu, D.S. Wu, T.C. An, Y. Wang, S. Dai, Intra-crystalline mesoporous zeolite encapsulation-derived thermally robust metal nanocatalyst in deep oxidation of light alkanes, Nat. Commun. 13 (2022) 295.

[8] X.F. Wang, A. Prévoteau, K. Rabaey, Impact of periodic polarization on groundwater denitrification in bioelectrochemical systems, Environ. Sci. Technol. 55 (2021) 15371–15379.

[9] J.P. You, J. Yu, S.H. Zhang, J.M. Chen, D.Z. Chen, Performance and mechanism of innovative two-phase partitioning microbial fuel cell for effective propanethiol treatment, Chem. Eng. J. 453 (2023), 139731.

[10] A. Kumar, T. Bhattacharya, W.A. Shaikh, A. Roy, S. Chakraborty, M. Vithanage, J. K. Biswas, Multifaceted applications of biochar in environmental management: a bibliometric profile, Biochar 5 (2023) 11.

[11] S.H. Zhang, J.P. You, C. Kennes, Z.W. Cheng, J.X. Ye, D.Z. Chen, J.M. Chen, L. D. Wang, Current advances of VOCs degradation by bioelectrochemical systems: a review, Chem. Eng. J. 334 (2018) 2625–2637.

[12] S. Li, C. Cheng, A. Thomas, Carbon-based microbial-fuel-cell electrodes: from conductive supports to active catalysts, Adv. Mater. 29 (2017), 1602547.

[13] J. Ye, Y.P. Chen, C. Gao, C. Wang, A.D. Hu, G.W. Dong, Z. Chen, S.G. Zhou, Y. J. Xiong, Sustainable conversion of microplastics to methane with ultrahigh selectivity by biotic–abiotic hybrid photocatalytic system, Angew. Chem. Int. Ed. 61 (2022), e202213244.

[14] W.J. Tian, H.Y. Zhang, X.G. Duan, H.Q. Sun, G.S. Shao, S.B. Wang, Porous carbons: structure-oriented design and versatile applications, Adv. Funct. Mater. 30 (2020), 1909265.

[15] P. Li, S. Kim, J. Jin, D.H. Chun, J.H. Park, Efficient photodegradation of volatile organic compounds by iron-based metal-organic frameworks with high adsorption capacity, Appl. Catal. B: Environ. 263 (2020), 118284.

[16] X. Liu, S.Y. Zhuo, X.Y. Jing, Y. Yuan, C. Rensing, S.G. Zhou, Flagella act as *Geobacter* biofilm scaffolds to stabilize biofilm and facilitate extracellular electron transfer, Biosens. Bioelectron. 146 (2019), 111748.

[17] F. Poiana, C. von Ballmoos, N. Gonska, M.R.A. Blomberg, P. Ädelroth, P. Brzezinski, Splitting of the O-O bond at the heme-copper catalytic site of respiratory oxidases, Sci. Adv. 3 (2017), e1700279.

[18] J.X. Tao, Q.L. Zhang, Y.H. Zhao, H.A. Chen, W.M. Liu, Y.Z. He, Y.N. Yin, T.Y. He, J. Chen, X.F. Wang, D.S. Wu, H.G. Peng, Elucidating the role of confinement and shielding effect over zeolite enveloped Ru catalysts for propane low temperature degradation, Chemosphere 302 (2022).

[19] Q. Li, D.Z. Chen, H.C. Jin, Q.G. Chen, Y. Yu, X.M. Chen, Periodic bipolar operation of $Ti/RuO_2-IrO_2-RhO_x$ electrodes for in-situ polymeric product desorption in recalcitrant contaminant degradation: from pseudocapacitive stabilization to model simulation, Chem. Eng. J. 448 (2022), 137497.

[20] S. Gao, W.L. Cen, Q. Li, J.Y. Li, Y.F. Lu, H.Q. Wang, Z.B. Wu, A mild one-step method for enhancing optical absorption of amine-functionalized metal-organic frameworks, Appl. Catal. B: Environ. 227 (2018) 190–197.

[21] X.D. Du, W.Y. Fu, P. Su, J.J. Cai, M.H. Zhou, Internal-micro-electrolysis-enhanced heterogeneous electro-Fenton process catalyzed by $Fe/Fe_3C@PC$ core–shell hybrid for sulfamethazine degradation, Chem. Eng. J. 398 (2020), 125681.

[22] H. Wang, Y. Shao, S.L. Mei, Y. Lu, M. Zhang, J.K. Sun, K. Matyjaszewski, M. Antonietti, J.Y. Yuan, Polymer-derived heteroatom-doped porous carbon materials, Chem. Rev. 120 (2020) 9363–9419.

[23] K. Liu, M.L. Yu, H.Y. Wang, J. Wang, W.P. Liu, M.R. Hoffmann, Multiphase porous electrochemical catalysts derived from iron-based metal–organic framework compounds, Environ. Sci. Technol. 53 (2019) 6474–6482.

[24] Z.W. Yang, X.Q. Xu, X.X. Liang, C. Lei, Y.H. Cui, W.H. Wu, Y.X. Yang, Z. Zhang, Z. Q. Lei, Construction of heterostructured $MIL-125/Ag/g-C_3N_4$ nanocomposite as an efficient bifunctional visible light photocatalyst for the organic oxidation and reduction reactions, Appl. Catal. B: Environ. 205 (2017) 42–54.

[25] A. Upadhyay, L. Zhu, F. Ren, R. Tehrani, Biosynthesis of conductive and paramagnetic value-added rare earth graphitic materials, Resour. Conserv. Recy. 189 (2023), 106737.

[26] Y.L. Yang, H.L. Ren, P. Ben Tzvi, X.L. Yang, Z. He, Optimal interval of periodic polarity reversal under automated control for maximizing hydrogen production in microbial electrolysis cells, Int. J. Hydrog. Energy 42 (2017) 20260–20268.

[27] D. Ki, P. Parameswaran, S.C. Popat, B.E. Rittmann, C.I. Torres, Effects of pre-fermentation and pulsed-electric-field treatment of primary sludge in microbial electrochemical cells, Bioresour. Technol. 195 (2015) 83–88.

[28] A.R. Hari, K. Venkidusamy, K.P. Katuri, S. Bagchi, P.E. Saikaly, Temporal microbial community dynamics in microbial electrolysis cells–influence of acetate and propionate concentration, Front. Microbiol. 8 (2017) 1371.

[29] T.H.J.A. Sleutels, H.V.M. Hamelers, C.J.N. Buisman, Effect of mass and charge transport speed and direction in porous anodes on microbial electrolysis cell performance, Bioresour. Technol. 102 (2011) 399–403.

[30] H.J. Mansoorian, A. Mahvi, R. Nabizadeh, M. Alimohammadi, S. Nazmara, K. Yaghmaeian, Evaluating the performance of coupled MFC-MEC with graphite felt/MWCNTs polyscale electrode in landfill leachate treatment, and bioelectricity and biogas production, J. Environ. Health Sci. 18 (2020) 1067–1082.

[31] H.S. Lee, B.E. Rittmann, Significance of biological hydrogen oxidation in a continuous single-chamber microbial electrolysis cell, Environ. Sci. Technol. 44 (2010) 948–954.

[32] N.I. Madondo, E. Kweinor Tetteh, S. Rathilal, B.F. Bakare, Effect of an electromagnetic field on anaerobic digestion: comparing an electromagnetic system (ES), a microbial electrolysis system (MEC), and a control with no external force, Molecules 27 (2022) 3372.

[33] C.W. Lin, C.Y. Tsao, S.L. Jiang, S.H. Liu, Enhanced gaseous ethyl acetate degradation and power generation by a bioelectrochemical system, Chem. Eng. J. 344 (2018) 270–276.

[34] A.G. Ramu, G. Muthuraman, I.S. Moon, Consistent room temperature electrochemical reduction of gaseous chlorobenzene to value-added intermediates by electroscrubbing, J. Ind. Eng. Chem. 89 (2020) 334–338.

[35] C.H. Wu, J.C. Shih, C.W. Lin, Continuous production of power using microbial fuel cells with integrated biotrickling filter for ethyl acetate-contaminated air stream treatment, Int. J. Hydrog. Energy 41 (2016) 21945–21954.

[36] M.F. Han, C. Wang, N.Y. Yang, X.R. Hu, Y.C. Wang, E.H. Duan, H.W. Ren, H.C. Hsi, J.G. Deng, Performance enhancement of a biofilter with pH buffering and filter bed supporting material in removal of chlorobenzene, Chemosphere 251 (2020), 126358.

[37] Q.W. Zhou, L.L. Zhang, J.M. Chen, B.C. Xu, G.W. Chu, J.F. Chen, Performance and microbial analysis of two different inocula for the removal of chlorobenzene in biotrickling filters, Chem. Eng. J. 284 (2016) 174–181.

[38] P.R. Joshi, S.C. Deshmukh, A.P. Morone, G. Kanade, R.A. Pandey, Air-lift reactor system for the treatment of waste-gas-containing monochlorobenzene, Environ. Technol. 34 (2013) 3023–3029.

[39] Z.Y. Ying, H. Chen, J.L. Gao, S.H. Zhang, R.J. Peng, J.P. You, J.M. Chen, J.K. Zhao, External potential regulated biocathode for enhanced removal of gaseous chlorobenzene in bioelectrchemical system, Chemosphere 274 (2021), 129990.

[40] Y.M. Li, K. Feng, C. Wu, J. Mei, S.H. Zhang, J.X. Ye, J.M. Chen, J.K. Zhao, J. R. Chen, Mass transfer and reaction simultaneously enhanced airlift microbial electrolytic cell system with high gaseous o-xylene removal capacity, Chemosphere 291 (2022), 132888.

[41] T.A.C. Oliveira, J.T. Scarpello, A.G. Livingston, Pervaporation-biological oxidation hybrid process for removal of volatile organic compounds from wastewaters, J. Membr. Sci. 195 (2002) 75–88.

[42] P. Sáez, A. Santos, R. García Cervilla, A. Romero, D. Lorenzo, Non-ionic surfactant recovery in surfactant enhancement aquifer remediation effluent with chlorobenzenes by semivolatile chlorinated organic compounds volatilization, Int. J. Environ. Res. Public Health 19 (2022) 7547.

[43] S.H. Zhang, J.P. You, N. An, J.K. Zhao, L.D. Wang, Z.W. Cheng, J.X. Ye, D.Z. Chen, J.M. Chen, Gaseous toluene powered microbial fuel cell: Performance, microbial community, and electron transfer pathway, Chem. Eng. J. 351 (2018) 515–522.

[44] H. Chen, Y.N. Yu, Y. Yu, J.X. Ye, S.H. Zhang, J.M. Chen, Exogenous electron transfer mediator enhancing gaseous toluene degradation in a microbial fuel cell: Performance and electron transfer mechanism, Chemosphere 282 (2021), 131028.

[45] M.F. Han, C. Wang, N.Y. Yang, Y.F. Li, X.R. Hu, E.H. Duan, Determination of filter bed structure characteristics and influence on performance of a 3D matrix biofilter in gaseous chlorobenzene treatment, Biochem. Eng. J. 165 (2021), 107829.

[46] Y. Yu, H.C. Jin, Q. Li, X.J. Zhang, Y. Zhang, X.M. Chen, Pseudocapacitive $Ti/RuO_2-IrO_2-RhO_x$ electrodes with high bipolar stability for phenol degradation, Sep. Purif. Technol. 263 (2021), 118395.

[47] H.C. Jin, Y. Yu, L. Zhang, R.X. Yan, X.M. Chen, Polarity reversal electrochemical process for water softening, Sep. Purif. Technol. 210 (2019) 943–949.

[48] H. Lin, H.J. Peng, X.W. Feng, X.J. Li, J.B. Zhao, K. Yang, J.B. Liao, D.M. Cheng, X. H. Liu, S.H. Lv, J.L. Xu, Q.G. Huang, Energy-efficient for advanced oxidation of bio-treated landfill leachate effluent by reactive electrochemical membranes (REMs): laboratory and pilot scale studies, Water Res 190 (2021), 116790.

[49] H.C. Jin, X.J. Zhang, Y. Yu, X.M. Chen, High-performance $Ti/IrO_2-RhO_x-TiO_2/\alpha-PbO_2/\beta-PbO_2$ electrodes for scale inhibitors degradation, Chem. Eng. J. 435 (2022), 135167.

[50] Z.M. Xiu, Q.B. Zhang, H.L. Puppala, V.L. Colvin, P.J.J. Alvarez, Negligible particle-specific antibacterial activity of silver nanoparticles, Nano Lett. 12 (2012) 4271–4275.

[51] S. Chen, Y. Zhou, J.Y. Li, Z.D. Hu, F. Dong, Y.X. Hu, H.Q. Wang, L.Z. Wang, K. K. Ostrikov, Z.B. Wu, Single-atom Ru-implanted metal–organic framework/MnO_2 for the highly selective oxidation of NO_x by plasma activation, ACS Catal. 10 (2020) 10185–10196.

[52] X.J. Yan, Q. Du, Q.H. Mu, L.L. Tian, Y.X. Wan, C.M. Liao, L.A. Zhou, Y.Q. Yan, N. Li, B.E. Logan, X. Wang, Long-term succession shows interspecies competition of *Geobacter* in exoelectrogenic biofilms, Environ. Sci. Technol. 55 (2021) 14928–14937.